

1 **Secondary aerosol formation under a special dust transport**
2 **event: impacts from unusually enhanced ozone and dust**
3 **backflows over the ocean**

4
5 Da Lu¹, Hao Li¹, Guochen Wang¹, Mengke Tian¹, Xiaofei Qin¹, Na Zhao¹, Juntao
6 Huo², Fan Yang³, Yanfen Lin², Jia Chen², Qingyan Fu², Yusen Duan², Xinyi Dong⁴,
7 Congrui Deng¹, Sabur F. Abdullaev⁵, Kan Huang^{1,6*}

8 ¹Center for Atmospheric Chemistry Study, Shanghai Key Laboratory of Atmospheric
9 Particle Pollution and Prevention (LAP³), National Observations and Research Station
10 for Wetland Ecosystems of the Yangtze Estuary, Department of Environmental
11 Science and Engineering, Fudan University, Shanghai, 200433, China

12 ²State Ecologic Environmental Scientific Observation and Research Station for
13 Dianshan Lake, Shanghai Environmental Monitoring Center, Shanghai, 200030,
14 China

15 ³Pudong New District Environmental Monitoring Station, Shanghai 200122, China

16 ⁴School of Atmospheric Sciences, Nanjing University, Nanjing 210023, China

17 ⁵Physical Technical Institute of the Academy of Sciences of Tajikistan, Dushanbe,
18 Tajikistan

19 ⁶Institute of Eco-Chongming (IEC), Shanghai, 202162, China

20 Corresponding author: huangkan@fudan.edu.cn

21

22 **Abstract**

23 In the autumn of 2019, a five-day long-lasting dust event was observed using a
24 synergy of field measurement techniques in Shanghai. This particular dust event stood

25 out from others due to its unique characteristics, including low wind speed, high relative
26 humidity, elevated levels of gaseous precursors, and contrasting wind patterns at
27 different altitudes. During this event, three distinct dust stages were identified. The first
28 stage was a typical dust invasion characterized by high concentrations of particulate
29 matters but relatively short duration. In contrast, the second stage exhibited an unusual
30 enhancement of ozone, attributed to compound causes of weak synoptic system,
31 transport from the ocean, and subsidence of high-altitude ozone down drafted by dust.
32 Consequently, gas phase oxidation served as the major formation pathway of sulfate
33 and nitrate. In the third stage of dust, a noteworthy phenomenon known as dust
34 backflow occurred. The dust plume originated from the Shandong Peninsula and slowly
35 drifted over the Yellow Sea and the East China Sea before eventually returning to
36 Shanghai. Evidence of this backflow was found through the enrichment of marine
37 vessel emissions (V and Ni) and increased solubility of calcium. Under the influence of
38 humid oceanic breezes, the formation of nitrate was dominated by aqueous processing.
39 Additionally, part of nitrate and sulfate were directly transported via sea salts,
40 evidenced by their co-variation with Na^+ and confirmed through thermodynamic
41 modeling. The uptake of NH_3 on particles, influenced by the contributions of alkali
42 metal ions and aerosol pH, regulated the formation potential of secondary aerosol. By
43 developing an upstream-receptor relationship method, the amounts of transported and
44 secondarily formed aerosol species were separated. This study highlights that the
45 transport pathway of dust, coupled with environmental conditions, can significantly
46 modify the aerosol properties, especially at the complex land-sea interface.

47

48 **1. Introduction**

49 Dust serves as a significant natural source of aerosols, constituting approximately
50 half of the tropospheric aerosols (Zheng et al., 2016). Dust aerosols play crucial roles
51 in environmental and climatic changes by affecting the radiation balance (Feng et al.,
52 2020; Nagashima et al., 2016; Goodman et al., 2019). The optical properties of dust
53 aerosols are influenced by various parameters of iron oxides, including refractive
54 indices, size distributions, and mineralogical compositions. Consequently, these factors
55 introduce potential uncertainties regarding the role of dust in climate forcing (Zhang et
56 al., 2015; Jeong, 2008). Furthermore, dust aerosols have important impacts on
57 tropospheric chemistry by participating in heterogeneous and photolysis reactions in
58 the atmosphere (Wang et al., 2014; Liu et al., 2018). During transport, dust can mix
59 with gaseous pollutants, toxic metals, and soot, thereby affecting air quality
60 immediately and potentially posing public health hazards (Liu et al., 2021; Wang et al.,
61 2021). Moreover, Barkley et al. (2021) found that iron-containing aerosols transported
62 from Africa to the equatorial North Atlantic Ocean provided plentiful nutrients to algae
63 in the ocean and accumulated inside algae.

64 The irregular shapes of dust particles provide an efficient medium for
65 heterogeneous reactions with NO_2 , O_3 , SO_2 , and NH_3 , thereby altering the particle size
66 spectrum, hygroscopicity, and radiative properties (Hsu et al., 2014; Tian et al., 2021;
67 Jiang et al., 2018). Jiang et al. (2018) observed a significant increase in nitrate and
68 sulfate concentrations during a dust period in March 2010 in Shanghai. This elevation
69 was attributed to the presence of moderate to high levels of relative humidity and
70 gaseous precursors, implying that dust can efficiently promote the formation of sulfate
71 and nitrate. Previous studies have revealed that HNO_3 formed through the reactions of
72 NO_2 with hydroxyl radical or N_2O_5 hydrolysis preferentially reacts with mineral dust

73 particles and produce nitrate, which serves as the primary source of nitrate during dust
74 episodes (Tang et al., 2016; Wu et al., 2020). Improvements in the simulation of sulfate
75 were achieved by employing various parameterization schemes for the heterogeneous
76 uptake of SO₂ on natural dust surfaces in the presence of NH₃ and NO₂ under different
77 relative humidity conditions (Zhang et al., 2019). Wang et al. (2018) simulated that
78 heterogeneous reactions on dust accounted for the majority of nitrate over the Yellow
79 Sea and the East China Sea during the dust long-range transport. Tang et al. (2017)
80 conducted a comprehensive review on the effect of dust heterogeneous reactions on the
81 tropospheric oxidation capacity. They proposed that high RH (> 80%) and a wider range
82 of temperature should be considered in the laboratory studies of heterogeneous
83 reactions of mineral dust. Additionally, more comprehensive kinetic models should be
84 developed to understand the complex multiphase reactions.

85 Controversies have arisen regarding the mixing of dust and anthropogenic aerosols.
86 Zhang et al. (2005) found that anthropogenic aerosols separated with dust during a dust
87 event in Qingdao, China. Coincidentally, a time-lag between dust and anthropogenic
88 aerosols was observed in Japan and South Korea downstream of the dust transport.
89 Single particle analysis revealed that sulfate in fine particles appeared 12 hours before
90 the dust arrival in Japan. Wang et al. (2013) also observed a lag of 10 - 12 hours between
91 dust and anthropogenic aerosols on a dust day in Shanghai (Wang et al., 2013).
92 Furthermore, Huang et al. (2019) documented vertical differences in long-transported
93 aerosols during a pollution event in Taiwan. Dust from the Gobi Desert in Inner
94 Mongolia and China existed at the altitudes of 0.8km and 1.90km, respectively, while
95 biomass burning aerosols from South Asia were present at higher altitudes of 3.5km.
96 Coastal regions often experience a mixture of inland anthropogenic emissions and

97 releases from the ocean, making regional pollution complex in these areas (Wang et
98 al.; Hilario et al., 2020; Patel and Rastogi, 2020; Perez et al., 2016; Wang et al., 2017).
99 The eastern coast of China, bordering the East China Sea and the Yellow Sea, is
100 particularly influenced by the Asian monsoon and high emissions from inland industries,
101 resulting in highly intricate meteorological and pollution conditions (Hilario et al.,
102 2020). Furthermore, the marine boundary layer in this region exhibits significant
103 seasonal and diurnal variations in , relative humidity and temperature further impacting
104 photochemical processes and heterogeneous reactions on aerosol surfaces (Zhao et al.,
105 2021). Sea and land breezes play a crucial role in this coastal area. During the night,
106 land breezes carry pollutants from the land to the sea. Subsequently, during the day,
107 these land breezes transform into sea breezes, bringing the pollutants back over the sea.
108 This phenomenon leads to an increase in air pollutants over the land (Zhao et al., 2021).
109 For instance, Wang et al. (2022b) found that during the ozone pollution in Shanghai in
110 2018, the presence of O₃ at high altitudes at night was transported vertically downward
111 during the daytime and high O₃ over the ocean was transported horizontally to the land,
112 jointly contributing to regional O₃ pollution in Shanghai. Also, one dust episode in 2014
113 was observed over Shanghai via detouring from northern China due to the blocked north
114 Pacific subtropical high-pressure system (Wang et al., 2018).

115 Previous studies have shown that about 70% of Asian dust traverses the eastern
116 coast of China before moving towards the Korean Peninsula, the Sea of Japan, and
117 eventually reaching the Pacific Ocean. The eastern coast of China serves as a crucial
118 route for Asian dust transport to the Pacific Ocean (Arimoto et al., 1997; Huang et al.,
119 2010). Most previous research has focused on typical dust events characterized by
120 strong intensities, high wind speed, low humidity, and low oxidants (Li et al., 2017; Ma

121 et al., 2019; Xu et al., 2017; Xie et al., 2005). In contrast, this study aims to depict an
122 atypical dust event that was observed in Shanghai, a coastal mega-city in Eastern China.
123 The unusualness of the meteorological conditions, transport pathways, and air
124 pollutants during the particular dust event was explicitly described. The study involves
125 categorizing the dust event into three stages and comparing the aerosol chemical
126 compositions between these stages. By focusing on the second and third stages, the
127 different formation mechanisms of nitrate and sulfate were investigated. The amounts
128 of major aerosol species from transport and secondary formation were estimated based
129 on a simplified method of relating the upstream and receptor simultaneous
130 measurements.

131

132 **2. Methodology**

133 **2.1. Observational sites**

134 At Shanghai Pudong Environmental Monitoring Station (31°13' N, 121°32'E),
135 comprehensive measurements of various atmospheric parameters were conducted.
136 All the instruments were installed on the top floor of a building, about 25m above
137 the ground level. As shown in Figure S1, the sampling site is situated at the eastern
138 tip of Shanghai, close to the coastal line. During November, the mean temperature
139 and relative humidity in Shanghai were recorded as 17.3°C and 72% respectively.
140 In autumn and winter, air pollutants originating from upstream urban regions often
141 undergo transport to Shanghai via high-pressure systems. Additionally, air
142 pollutants in Shanghai tended to linger at the sea/land boundary regions due to the
143 sea-land breeze (Shen et al., 2019).

144 In addition to the measurements taken in Shanghai, data from environmental
145 monitoring stations in Qingdao and Lianyungang are also incorporated into this
146 study.

147

148 **2.2. Instrumentation**

149 A set of online instruments was set up at the Pudong observational site. Inorganic ions
150 (NO_3^- , SO_4^{2-} , Cl^- , Na^+ , NH_4^+ , K^+ , Mg^{2+} , Ca^{2+}) in $\text{PM}_{2.5}$ and soluble gases (NH_3 , HNO_3 ,
151 HCl , HONO) were measured by an online ion chromatography (IC, MARGA-1S,
152 Metrohm). It operated at a flow rate of 16.7 L/min with a time resolution of one hour.
153 Briefly, air was drawn into a $\text{PM}_{2.5}$ cyclone inlet and passed through a wet rotating
154 denuder (gases) and a steam jet aerosol collector (aerosols). Subsequently, the aqueous
155 samples were analyzed with ion chromatography. More details can be found in (Xu et
156 al., 2020). Hourly trace metals (Si, Ca, Cu, Fe, K, Co, Mn, Cr, Zn, Pb, As, Cd, V, Ni) in
157 $\text{PM}_{2.5}$ were measured by using the Xact 625 multi-metals monitor (Cooper
158 Environmental, Beaverton, OR, USA). Particles were collected onto a Teflon filter tape
159 at a flow rate of 16.7 L/min, and then transported into the spectrometer where the
160 particles were analyzed with an X-ray fluorescence. Organic carbon and elemental
161 carbon were measured by an in situ Semi-Continuous Organic Carbon and Elemental
162 Carbon aerosol analyzer (RT-4, Sunset Laboratory, Beaverton, Oregon, USA). Samples
163 were collected for 40 min and then analyzed in the following 20 min. The concentration
164 of mineral aerosols is calculated by summing the major mineral elements with oxygen
165 for their normal oxides, i.e., $[\text{Minerals}] = (2.2 \cdot \text{Al} + 2.49 \cdot \text{Si} + 1.63 \cdot \text{Ca} + 2.42 \cdot \text{Fe} + 1.94 \cdot \text{Ti})$
166 (Malm et al., 1994). The concentration of OM (organic matters) is estimated by
167 multiplying OC with a factor of 2.

168 The concentrations of particles and gaseous pollutants were measured by a set of
169 Thermo Fisher Scientific instruments, including PM_{2.5} (Thermo 5030i), PM₁₀ (Thermo
170 5030i), SO₂ (Thermo Fisher 43i), NO_x (Thermo Fisher 42i), O₃ (Thermo Fisher 49i),
171 and CO (Thermo Fisher 48i-TLE). These parameters were measured at the temporal
172 resolution of 5min. Meteorological parameters (ambient temperature, relative humidity,
173 wind speed, and wind direction) were obtained by a Vaisala Weather transmitter
174 (WXT520) at the temporal resolution of 1min. The height of planetary boundary layer
175 (PBL) was retrieved from a ceilometer (CL31, Vaisala) at the temporal resolution of 30
176 min. Vertical profiles of aerosol optical properties were obtained by an aerosol lidar
177 (AGJ, AIOFM) at the temporal resolution of 30 min and vertical resolution of 7.5 m,
178 respectively. Vertical profiles of ozone were obtained by an ozone lidar (LIDAR-G-
179 2000, WUXIZHONGKE) at the temporal resolution of 15 min and vertical resolution
180 of 7.5 m, respectively. All instruments are routinely maintained and calibrated to ensure
181 the quality of data.

182

183 **2.3. Thermodynamic simulation of aerosol pH and aerosol liquid water content**

184 The ISORROPIA II model is subject to the principle of minimizing the Gibbs energy
185 of the multi-phase aerosol system, leading to a computationally intensive optimization
186 problem (Song et al., 2018). The model can predict the physical state and compositions
187 of atmospheric inorganic species (NH₄⁺, Na⁺, K⁺, Mg²⁺, Ca²⁺, SO₄²⁻, NO₃⁻ and Cl⁻)
188 with their gas- and particle-phase concentrations and meteorological parameters
189 (relative humidity and temperature) as model inputs. The model includes two modes,
190 i.e., reverse and forward mode. The reverse mode calculates the equilibrium
191 partitioning based on aerosol-phase concentrations only, while the latter uses both

192 aerosol-phase and gas-phase concentrations as inputs. Moreover, particles can be
193 assumed as “metastable” with liquid-phase but no solid participating while “stable”
194 with the liquid and solid phases or both. The ISORROPIA running in the forward mode
195 at the metastable state was applied in this study. Aerosol pH was calculated based on
196 the equilibrium particle hydronium ion concentration and aerosol liquid water content
197 (ALWC) obtained from model results. The performances and advantages of
198 ISORROPIA over the usage of other thermodynamic equilibrium codes has been
199 assessed in numerous studies (Nenes et al., 1998; West et al., 1999; Ansari and Pandis,
200 1999; Yu et al., 2005).

201

202 **2.4. Hybrid Single-Particle Lagrangian Integrated Trajectory Model**

203 The HYSPLIT (Hybrid Single-Particle Lagrangian Integrated Trajectory) was
204 used to compute the backward trajectories of the air parcels during the dust events. It is
205 a widely used model that computes dispersion following the particle or puff. The
206 advection of a particle or puff is computed from the average of the three-dimensional
207 velocity vectors for the initial position and the first-guess position (Draxler
208 and Hess, 1998). Turbulent velocity components are expressed as a function of the
209 velocity variance, a statistical quantity derived from the meteorological data, and the
210 Lagrangian time scale. The calculation of air mass trajectories can be used to depict the
211 airflow patterns for interpreting the transport of air pollutants over various spatial and
212 temporal ranges (Stein et al., 2015). In this study, the HYSPLIT model was driven by
213 meteorological data outputs from the Global Data Assimilation System (GDAS) (Su et
214 al., 2015), which is available at <ftp://arlftp.arlhq.noaa.gov/pub/archives/gdas1>. Air mass
215 trajectories were launched at different heights from the ground and a total duration of

216 48 hours simulation was conducted.

217

218 **2.5. Calculation of uptake coefficient of NH₃ (γ_{NH_3}) on particles**

219 NH₃, being the most abundant alkaline species in the atmosphere, plays a crucial
220 role in acid neutralization and secondary aerosol formation. To assess the gas-particle
221 partitioning of NH₃, the uptake coefficient of NH₃ (γ_{NH_3}) on particles is calculated as
222 below. Initially, the quasi-first-order reaction rate constant for heterogeneous
223 conversion from NH₃ to NH₄⁺ (k_{het} , s⁻¹) is calculated is calculated by Eq. (1) (Liu et
224 al., 2022).

$$225 \quad k_{\text{het}} = \frac{2(C_{\text{NH}_4^+,t_2} - C_{\text{NH}_4^+,t_1})}{(C_{\text{NH}_3,t_2} + C_{\text{NH}_3,t_1})(t_2 - t_1)} \quad (1)$$

226 k_{het} is only valid when $c_{\text{NH}_4^+}$ increases, while c_{NH_3} decreases assuming a constant
227 emission rate from t_1 to t_2 (1 h in this study). Then, the uptake coefficient of NH₃ (γ_{NH_3})
228 on particles can be calculated as below (Liu et al., 2022; Wang and Lu, 2016).

$$229 \quad \gamma_{\text{NH}_3} = \frac{4k_{\text{het}}}{S\omega} = \frac{4k_{\text{het}}}{S\sqrt{\frac{8RT}{\pi M}}} \quad (2)$$

230 where S is the surface area of particles (m² m⁻³) measured using SMPS and APS. ω is
231 the velocity of NH₃ molecules. T is the ambient temperature (K). R is the ideal gas
232 constant, and M is the molecular weight of NH₃ (kg mol⁻¹).

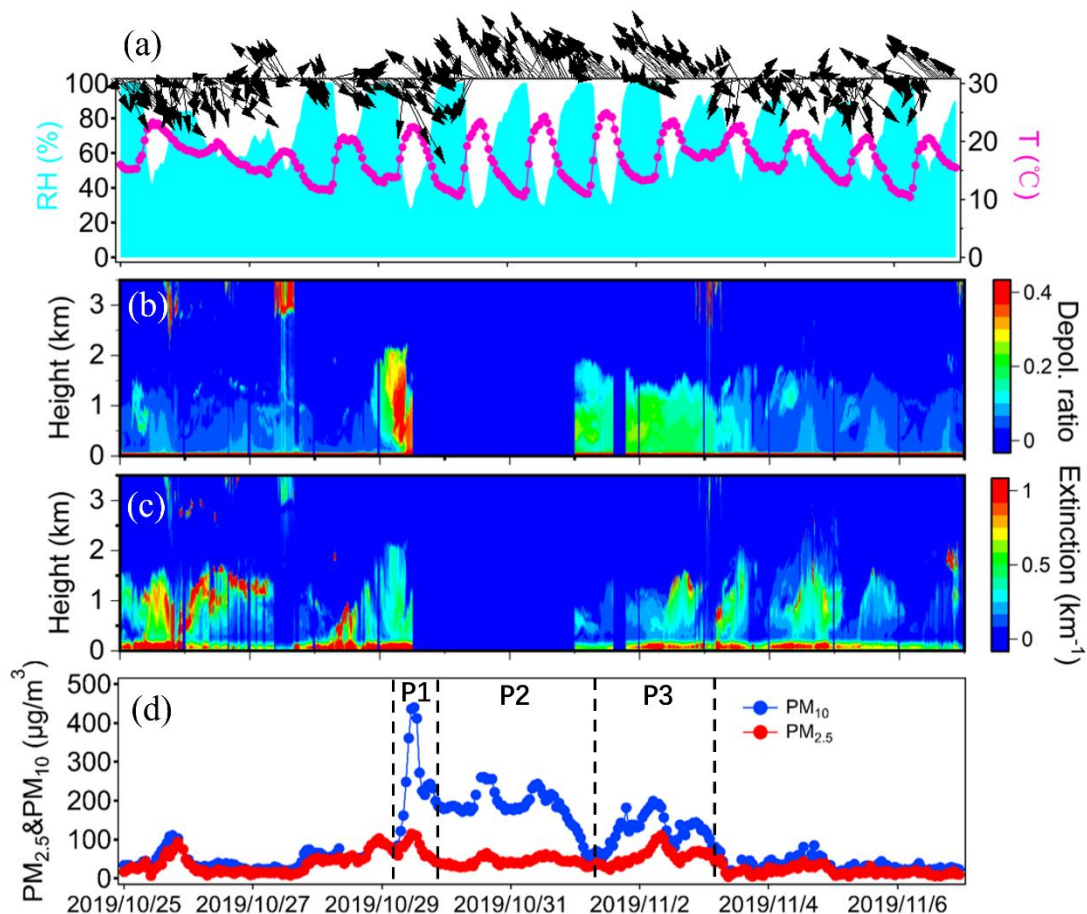
233

234 **3. Results and Discussion**

235 **3.1. Characteristics of an unusual dust event**

236 Figure 1 shows the time series of PM₁₀, PM_{2.5}, meteorological parameters, as well
237 as the vertical profiles of aerosol extinction coefficient and depolarization ratio
238 observed at the Shanghai sampling site from October 25 to November 6, 2019. From
239 October 25 to 28, the mean wind speed was 0.9±0.72m/s with a peak value of 3.1m/s,

240 remaining relatively low, and predominantly blowing from the northwest. The mean
241 concentrations of $PM_{2.5}$ and PM_{10} were 34.7 and $44.2 \mu\text{g}/\text{m}^3$, respectively. Starting at
242 4:00 LST on October 29, the concentration of PM_{10} increased sharply and lasted till
243 November 2 (Figure 1d). The aerosol lidar observation indicated that both the aerosol
244 extinction coefficient and depolarization ratio extended from the ground to around 2km
245 during the same period. In general, if the particle depolarization ratio exceeds 10%, the
246 aerosol is identified as mineral dust (Shimizu et al., 2004) due to the nonsphericity
247 (irregular shapes) and relatively large size of particles (Mcneil and Carswell, 1975).
248 Notably, the enhanced depolarization ratio (>0.1) suggested the occurrence of a
249 prolonged dust event in Shanghai. By using the $PM_{2.5}/PM_{10}$ mass ratio of 0.4 as a
250 threshold (Fan et al., 2021), the period from October 29 to November 2 was defined as
251 the dust period in this study. The remaining days, including October 25 to October 28
252 and November 3 to November 6, were defined as the non-dust period. Throughout the
253 entire dust period, the mean concentrations of $PM_{2.5}$ and PM_{10} reached $53.3 \pm$
254 $20.5 \mu\text{g}/\text{m}^3$ and $172.4 \pm 70.2 \mu\text{g}/\text{m}^3$, respectively, yielding a low $PM_{2.5}/PM_{10}$ ratio of 0.34
255 ± 0.15 . As a comparison, $PM_{2.5}$ and PM_{10} during the non-dust period was $38.9 \mu\text{g}/\text{m}^3$
256 and $49.8 \mu\text{g}/\text{m}^3$, respectively, exhibiting a relatively high $PM_{2.5}/PM_{10}$ ratio of 0.62 ± 0.20 .
257



258

259 Figure 1. Time series of (a) relative humidity, temperature, wind vectors, (b) aerosol
 260 depolarization ratio, (c) aerosol extinction coefficient, (d) mass concentrations of PM_{2.5}
 261 and PM₁₀ during the study period. Three dust stages, i.e., P1, P2, and P3 are also marked.
 262 The missing aerosol lidar data were due to instrument malfunction.

263

264 The occurrences of dust are typically accompanied by low relative humidity and
 265 strong winds due to the passage of cold fronts (Huang et al., 2010; Wang et al., 2013;
 266 Wang et al., 2018). However, in this study, relative humidity was exceptionally high
 267 with the mean value of $71 \pm 26\%$. It showed strong diurnal variation, reaching its
 268 minimum in the daytime and even close to 100% in the nighttime (Figure 1a).
 269 Additionally, wind speed was low of 0.54 ± 0.59 m/s with a maximum of 2.6 m/s. This
 270 stagnant synoptic condition led to elevated concentrations of main gaseous pollutants

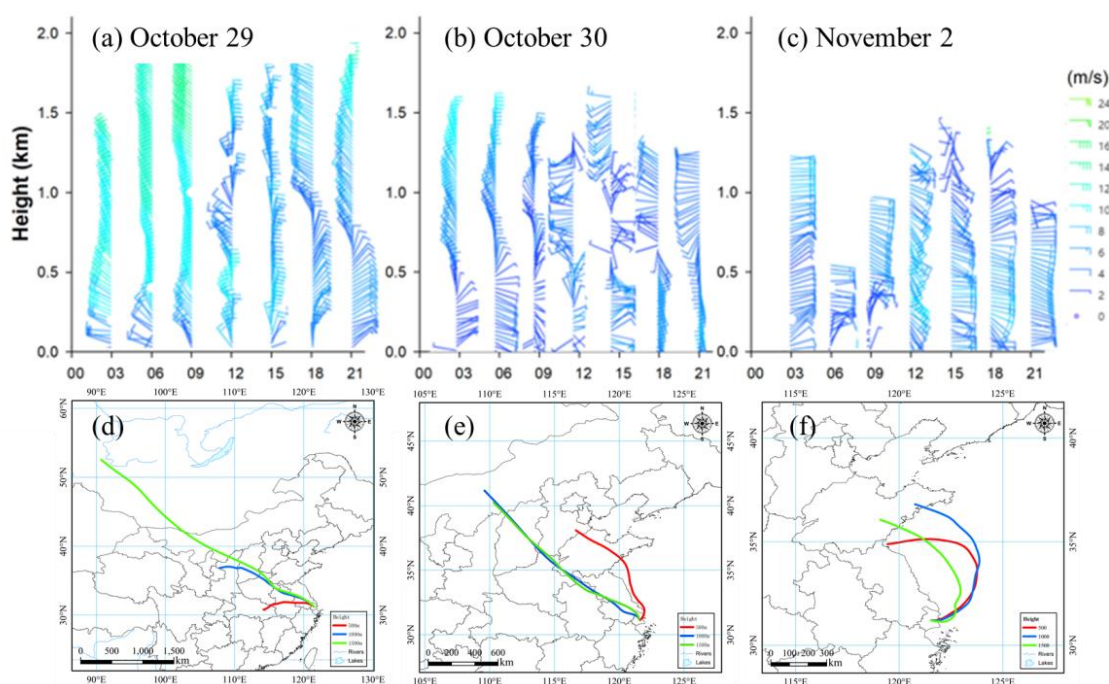
271 such as O₃, SO₂, and NO₂, with mean values of 86.0±47.8μg/m³, 11.8±3.4μg/m³, and
272 63.3±27.9μg/m³, respectively, even higher than those during the non-dust period.

273 We further divided the dust event into three stages based on the temporal
274 characteristics of PM₁₀ and the transport patterns of air masses. As shown in Figure 1d,
275 PM₁₀ quickly climbed from 4:00 on October 29 and reached a maximum of 436μg/m³
276 after 8 hours. The air masses primarily originated from the semi-arid regions of
277 northwest China (Figure 2d), which was consistent with both the near surface wind
278 observation (Figure 1a) and wind lidar observation (Figure 2a). The wind profiles
279 showed prevailing northwest winds from the surface up to around 2km before noon on
280 October 29, indicating the presence of a strong synoptic system. Afterwards, PM₁₀
281 quickly decreased to 199 μg/m³ at 20:00, October 29 within 8 hours. This was primarily
282 attributed to the shift of wind directions. As shown in Figure 2a, while winds above
283 700m continued to blow from the northwest, near- surface winds had shifted from the
284 southeast. Due to Shanghai's coastal location adjacent to the East China Sea, the
285 relatively clean southeasterlies diluted the local air pollutants, thereby explaining the
286 quick decline in PM₁₀ concentrations. This initial dust episode occurring from 4:00 -
287 13:00 on October 29 was defined as Stage P1.

288 Despite the persistent southeasterly winds, the dust event did not come to a
289 complete halt. Even under these prevailing winds, hourly PM₁₀ concentrations
290 remained above 150 μg/m³ until November 1, gradually decreasing to 65 μg/m³ at 03:00,
291 November 1 (Figure 1d). Compared to P1, wind speed during this stage was as low as
292 0.4 ± 0.5m/s, while RH was moderately high of 70 ± 26%. Although the daytime RH
293 stayed low between 30% and 50%, it frequently soared above 90% at nighttime. Figure
294 2e shows that although the air masses originated from the Gobi Desert, they also

295 traversed considerable coastal regions. The wind profiles further indicated that while
296 northwest winds prevailed at altitudes higher than 500m, east and northeast winds were
297 dominant below 500m (Figure 2b). Consequently, the relatively high RH during this
298 period can be attributed to the mixing of dust plumes with coastal sea breezes. This dust
299 episode from 14:00, October 29 to 3:00 on November 1 was designated as Stage P2.

300 Following P2, PM₁₀ and PM_{2.5} rose again and peaked at 5:00 and 9:00 on
301 November 2 with the hourly concentration of 199 and 117 $\mu\text{g}/\text{m}^3$, respectively. Different
302 from P1 and P2, the air masses during this stage originated from the Shandong
303 Peninsula and the northern region of Jiangsu province, and then migrated over the
304 Yellow Sea and the East China Sea (Figure 2f). Typically, dust plumes tend to travel
305 eastward, impacting the western Pacific region and even distant oceanic regions (Wang
306 et al., 2018; Nagashima et al., 2016). However, in this case, the air masses evidently
307 deviated and pushed the dust back towards the mainland. The wind profiles on
308 November 2 revealed that winds within the detected altitude range predominantly
309 originated from the eastern and southeastern oceanic regions (Figure 2c). This probably
310 indicated the mixing between dust plumes and humid oceanic air masses was quite
311 sufficient, which was also reflected by the highest average RH of $76 \pm 24\%$ among the
312 three stages of the dust event. Moreover, the concentrations of O₃ and NO₂ at this stage
313 were higher than those of P1 and P2, potentially promoting the formation of secondary
314 aerosol components and will be discussed later. This rarely observed dust backflow
315 transport episode from 4:00 on November 1 to 23:00 on November 2 was designated
316 as Stage P3.



317

318 Figure 2. Wind profiles observed by a wind profiler radar on (a) October 29, (b) October
 319 30, and (c) November 2. 48-hour backward trajectories simulated at the sampling site
 320 starting from (d) 4:00 AM, October 29, (e) 9:00 AM, October 30, and (f) 13:00 PM,
 321 November 2. The red, blue, and green trajectories represented starting altitudes of 100,
 322 500, and 1500m, respectively.

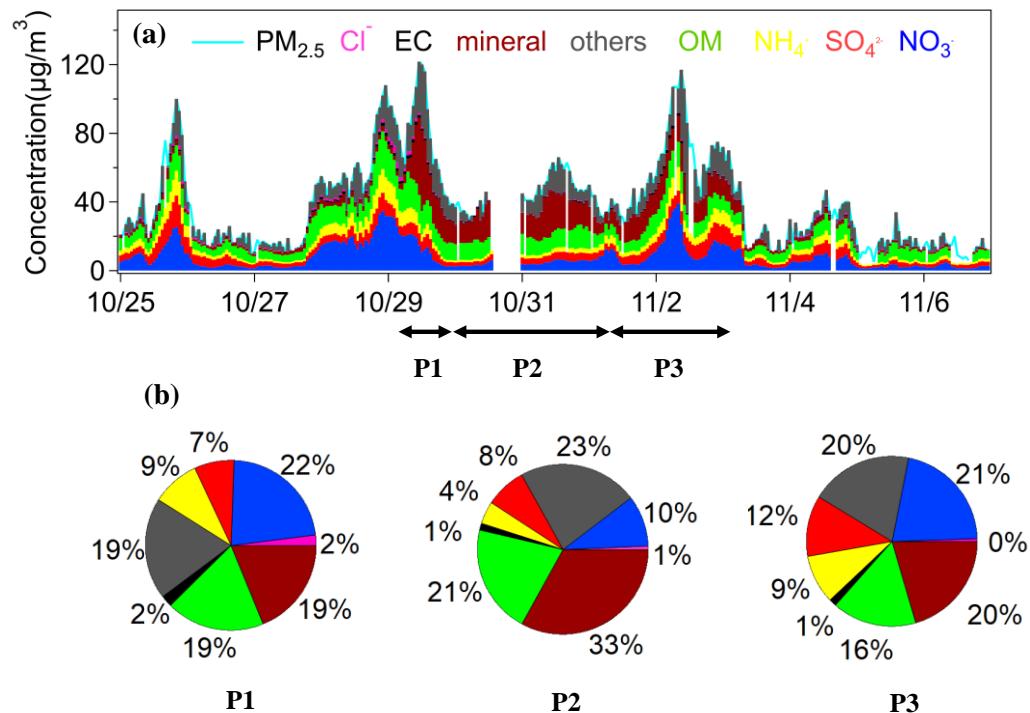
323

324 3.2. Comparisons of aerosol chemical compositions among the three dust stages

325 Figure 3a shows the time-series of hourly aerosol chemical components,
 326 including SNA (NO_3^- , SO_4^{2-} , and NH_4^+), OM, EC, and mineral aerosols in $\text{PM}_{2.5}$.
 327 During P1, the mean concentration of SNA was $49.9 \pm 31.6 \mu\text{g}/\text{m}^3$. The mineral
 328 aerosols reached $16.4 \pm 14.6 \mu\text{g}/\text{m}^3$, accounting for 19% in $\text{PM}_{2.5}$. The contribution of

329 OM to PM_{2.5} was almost identical to that of mineral aerosols (Figure 3b).

330



331

332 Figure 3. (a) Times-series of major chemical components in PM_{2.5} during the study
 333 period. (b) The mean proportion of major chemical components in PM_{2.5} during the
 334 three dust stages.

335

336 During P2, mineral aerosols increased to $23.4 \pm 54.1 \mu\text{g}/\text{m}^3$ and accounted for 33%
 337 in PM_{2.5}, representing the highest among all three stages (Figure 3b). Due to the
 338 continuous dilution effect of dust on local anthropogenic pollutants, the concentrations
 339 and proportions of SNA in PM_{2.5} were the lowest during this stage. For instance, NO₃⁻
 340 only accounted for 10% in PM_{2.5}, indicating a suppression of nitrate formation to some
 341 extent. The levels of OM didn't exhibit obvious changes and averaged $10.1 \pm 2.1 \mu\text{g}/\text{m}^3$,
 342 accounting for 21% in PM_{2.5}.

343 During P3, mineral aerosols averaged $11.9 \pm 2.7 \mu\text{g}/\text{m}^3$, ranking the lowest among
 344 all three stages. The proportion of mineral aerosols in PM_{2.5} decreased to 20%,

345 suggesting the dust backflow from the ocean was less enriched in mineral components.
346 Compared to P2, SNA showed significant increases and much stronger diurnal
347 variations during P3. SO_4^{2-} , NO_3^- , and NH_4^+ averaged 6.7 ± 2.4 , 12.4 ± 8.9 , and $5.4 \pm$
348 $2.7 \mu\text{g}/\text{m}^3$, respectively. As shown in Figure 3b, the contribution of nitrate to $\text{PM}_{2.5}$
349 increased to 21%, while that of sulfate rose to 12%, the highest among all three stages.
350 The concentration of OM ($9.3 \pm 3.2 \mu\text{g}/\text{m}^3$) and its proportion (16%) during P3 were
351 lower than the other two stages, likely due to the unconventional dust backflow
352 transport pathway.

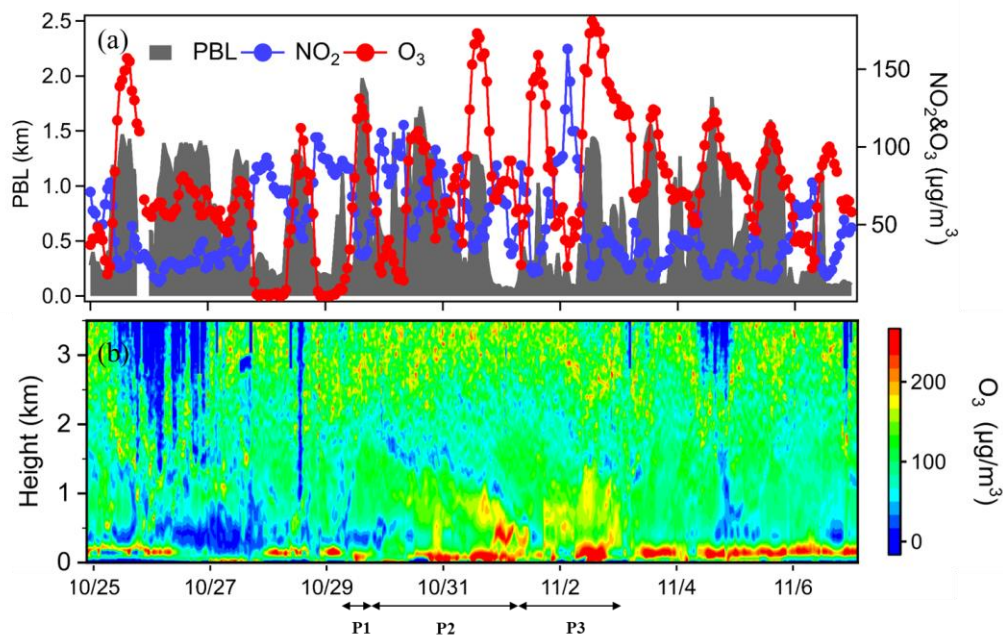
353

354 **3.3. Unconventional features of the dust episodes**

355 **3.3.1. Unusually enhanced O_3 during dust**

356 Figure 4 shows the hourly near surface ozone concentrations and vertical profiles
357 of ozone during the study period. Interestingly, a few high O_3 peaks occurred during
358 the dust event (Figure 4a). O_3 averaged $92.8 \pm 52.8 \mu\text{g}/\text{m}^3$ during the dust, about 50%
359 higher than the non-dust days. Among the three dust stages, O_3 substantially increased
360 from $35.9 \pm 36.4 \mu\text{g}/\text{m}^3$ during P1 to $80.7 \pm 41.2 \mu\text{g}/\text{m}^3$ during P2, and further rose to
361 $104.0 \pm 48.7 \mu\text{g}/\text{m}^3$ during P3. The low O_3 during P1 can be attributed to the cleansing
362 effect of the strong dust associated with the cold front, which was consistent with
363 previous studies that reported reduced oxidant concentrations during intense dust
364 events (Benas et al., 2013). Regarding the relatively high O_3 during P2 and P3, several
365 causes may contribute to this phenomenon. Firstly, the mean wind speed was low of
366 0.4 and 0.6 m/s during P2 and P3, respectively. One numerical study conducted
367 during the similar period suggested that the low wind speed caused reduction of
368 boundary layer height and the warming of the lower atmosphere, thus accelerating the

369 ozone formation by ~ 1 ppbv/h (Wang et al., 2020). Consequently, this weak synoptic
 370 system was favorable for the accumulation of ozone. Secondly, since the dust plume
 371 travelled mostly over the coastal and oceanic areas, a portion of O_3 could be
 372 transported from the high ozone oceanic areas (Wang et al., 2022b). Thirdly, the
 373 ozone lidar also detected high O_3 stripes during P2 and P3. As shown in Figure 4b, the
 374 high O_3 profiles extended from the surface to around 1km and the profile structure
 375 was similar to that of aerosol depolarization ratio. The subsidence of dust particles
 376 likely contributed to downward transport of high-altitude O_3 , thereby influencing the
 377 elevated O_3 near the ground (Yang et al., 2022).



378
 379 Figure 4. (a) Time-series of near surface O_3 , NO_2 and planetary boundary layer height
 380 (b) Vertical profiles of ozone observed by the ozone Lidar.

381

382 3.3.2. Dust backflows during P3

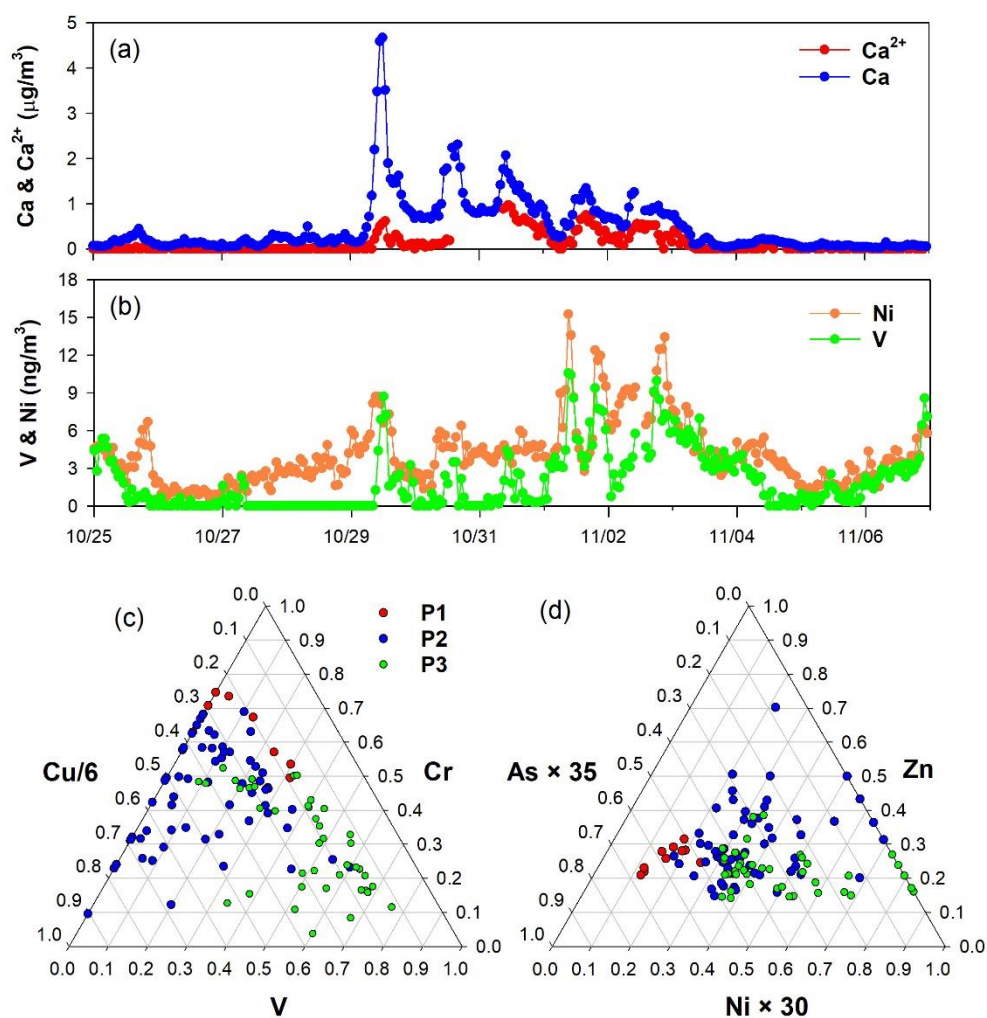
383 The dust during P3 was diagnosed as a backflow transport pathway from the
 384 mainland to Shanghai through the Yellow Sea and the East China Sea, as determined
 385 by the backward trajectory analysis (Figure 2f). This unconventional dust transport

386 route, termed “dust backflow”, was consistent with a similar occurrence in 2014 when
387 dust from northern China detoured over Shanghai (Wang et al., 2018). In this section,
388 we have provided further evidences of the dust backflow from various aspects.

389 Figure 2f illustrates that the dust drifted away from the Shandong Peninsula, thus
390 we selected two coastal sites in Shandong province for supplementary analysis. Figure
391 S2 compares the time-series of hourly air pollutants at Qingdao, Lianyungang, and
392 Shanghai. At Qingdao and Lianyungang, high PM₁₀ concentrations were observed
393 during October 30 – 31, indicating the invasion of dust in these regions. After about
394 two days, PM₁₀ peaked in Shanghai on early November 2. This temporal consistency
395 aligned with the simulation duration of the backward trajectories, which lasted around
396 48 hours (Figure 2f). In Figure 9, it can be observed that in the upstream dust regions
397 (i.e., Qingdao and Lianyungang), PM₁₀ varied negatively with NO₂ and CO (the
398 highlighted period in the figure). While in Shanghai, positive correlations between
399 PM₁₀ and both NO₂ ($R^2=0.32$) and CO ($R^2=0.55$) indicated that the dust during P3
400 served as a carrier for gaseous pollutants rather than acting a diluter.

401

402



403

404 Figure 5. Time-series of (a) Ca, Ca²⁺, (b) V, and Ni during the study period. (c)

405 Cu-Cr-V ternary diagram and (d) As-Zn-Ni ternary diagram among the P1 – P3 dust

406 episodes. Due to substantial concentration differences of various elements, some

407 elements are artificially changed to make most scatters appear around the centroid.

408

409 Additional evidence of dust backflows was provided from the perspective of

410 aerosol chemical tracers. Figure 5a plots the time-series of Ca and Ca²⁺, representing

411 the total calcium and the soluble part of calcium, respectively. It was observed that Ca

412 and Ca²⁺ didn't exhibit a proportional variation trend, which should be related to the

413 solubility of calcium during different dust stages. During P1, the mean concentration of
414 Ca reached the highest of $1.63 \pm 1.53 \mu\text{g}/\text{m}^3$ while Ca^{2+} was the lowest of $0.21 \pm$
415 $0.20 \mu\text{g}/\text{m}^3$, thus resulting in the lowest Ca^{2+}/Ca ratio of 0.10 ± 0.08 . As discussed in
416 Section 3.1, dust during P1 was the strongest and thus it contained higher fractions of
417 minerals, primarily in the form of insoluble metal oxides. The average concentrations
418 of Ca^{2+} and Ca during P2 were $0.33 \pm 0.28 \mu\text{g}/\text{m}^3$ and $1.11 \pm 0.46 \mu\text{g}/\text{m}^3$, respectively,
419 resulting in the higher Ca^{2+}/Ca ratio of 0.27 ± 0.20 . As a comparison, the average
420 concentrations of Ca^{2+} and Ca during P3 reached $0.34 \pm 0.20 \mu\text{g}/\text{m}^3$ and $0.78 \pm$
421 $0.27 \mu\text{g}/\text{m}^3$, respectively, yielding the highest Ca^{2+}/Ca ratio of 0.38 ± 0.19 . The
422 significantly higher solubility of calcium during P3 should be directly related to the
423 prolonged presence of dust plumes over the open ocean. The abundant water vapor over
424 the ocean could accelerate the dissolution of the insoluble components in particles
425 during the mixing between continental dust and oceanic air masses. Additionally, the
426 backflow transport pathway facilitated the entrainment of sea salts and contributed to
427 the increase of soluble calcium.

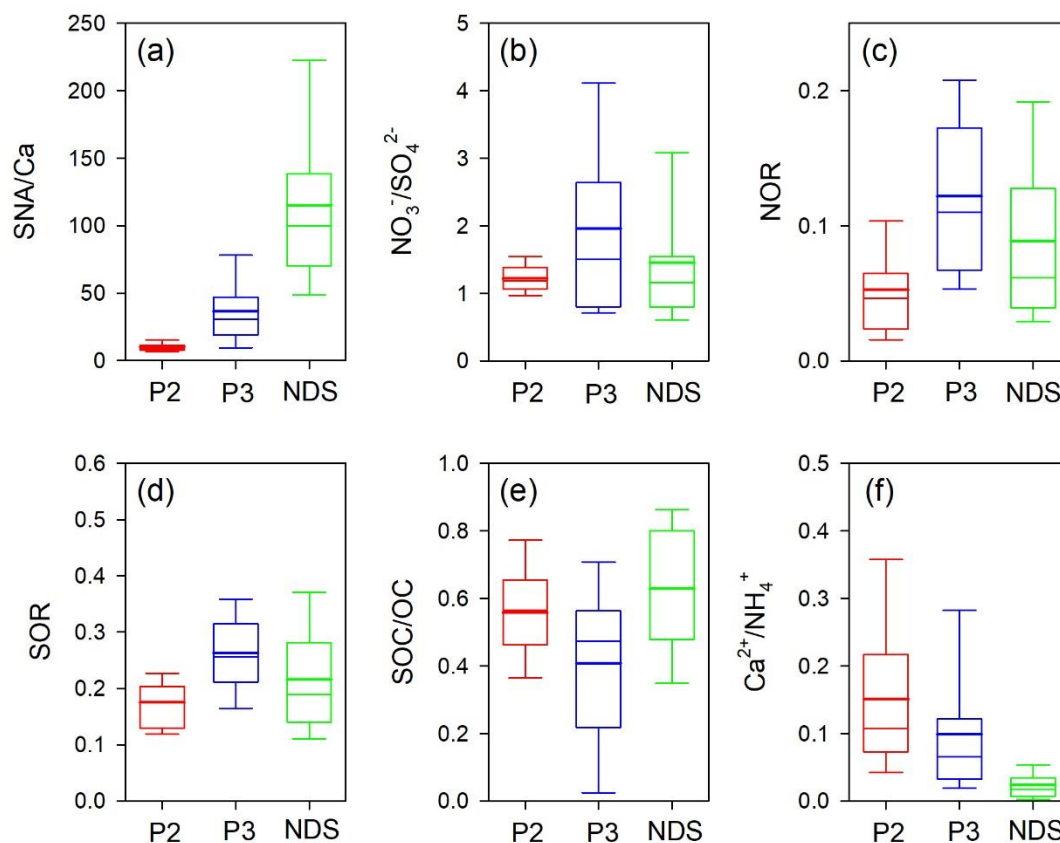
428 Figure 5b provides additional insights by displaying the time-series of V and Ni,
429 which are typical tracers of oil combustions (Becagli et al., 2012). They varied
430 significantly during the study period, and the mass concentrations of V and Ni increased
431 4 and 1.8 times during P3 compared to P2, respectively. Consistently, the enrichment
432 factors of Ni and V displayed higher values during P3 than P1 and P2 (Figure S3). The
433 trends are substantiated in the ternary diagrams, which are commonly applied to
434 illustrate the relative abundances of three components and infer the source variations
435 (Bozlaker et al., 2019; Cwiertny et al., 2008; Laskin et al., 2005). As shown in the Cu-
436 Cr-V ternary diagram (Figure 5c), the dust samples during P1 were positioned away

437 from the V-apex. As a comparison, the dust samples during P2 exhibited greater
438 scattering, manifesting enhanced anthropogenic contributions, e.g., from chrome
439 plating industries (Hammond et al., 2008). Compared to P2, the dust samples during P3
440 moved toward the V-apex, indicating a higher contribution from oil combustions
441 (Becagli et al., 2012). A similar pattern was observed in the As-Zn-Ni ternary diagram
442 (Figure 5d). The majority of dust samples during P2 spanned across the diagram,
443 reflecting contributions from mixed anthropogenic sources. Reciprocally, P3 was closer
444 to the Ni-apex. These lines of evidences collectively confirmed that the dust had mixed
445 with pollutants from marine vessel emissions over one of the busiest international
446 shipping trade routes (Fan et al., 2016) and was subsequently transported back to
447 Shanghai.

448

449 **3.4. Formation of secondary aerosols during the dust long-range transport**

450 **3.4.1. Comparison of typical chemical tracers**



451

452 Figure 6. Box plots of (a) SNA/Ca, (b) $\text{NO}_3^-/\text{SO}_4^{2-}$, (c) NOR, (d) SOR, (e) SOC/OC,
 453 and (f) $\text{Ca}^{2+}/\text{NH}_4^+$ during P2, P3, and NDS, respectively.

454

455 To delve deeper into the formation characteristics of secondary aerosols in
 456 different stages, a variety of chemical tracers was investigated. The P1 dust stage was
 457 excluded from statistical analysis due to its short duration and limited data availability.
 458 Figure 6a shows the comparison of SNA/Ca ratios during P2, P3 and non-dust days
 459 (NDS). The SNA/Ca ratio can be used to assess the relative changes between secondary
 460 production and primary dust emission by eliminating the impact of meteorological
 461 conditions among different periods (Zheng et al., 2015). Compared to the two dust
 462 episodes, the SNA/Ca ratio is significantly higher during NDS. This can be attributed
 463 to the much lower concentrations of mineral aerosols during NDS, thus resulting in the

464 higher SNA relative to Ca. In terms of comparing P2 and P3, the average SNA/Ca ratio
465 during P3 was 3 times that of P2, indicating that the formation of secondary inorganic
466 aerosols was more prominent during the dust backflow. Regarding the $\text{NO}_3^-/\text{SO}_4^{2-}$ ratios
467 (Figure 6b), they were close between NDS and P2, with NO_3^- slightly exceeding SO_4^{2-} .
468 The range of $\text{NO}_3^-/\text{SO}_4^{2-}$ was the largest during P3 with a mean value of around 2,
469 suggesting that the dust backflow was more conducive to the accumulation of nitrate.
470 The nitrogen oxidation ratio ($\text{NOR} = \text{NO}_3^-/(\text{NO}_3^- + \text{NO}_2)$) and the sulfur oxidation ratio
471 ($\text{SOR} = \text{SO}_4^{2-}/(\text{SO}_4^{2-} + \text{SO}_2)$) were further used to gauge the extent of nitrate and sulfate
472 formation, both showing trends of $\text{P3} > \text{NDS} > \text{P2}$ (Figure 6c & 6d). It should be noted
473 that NOR and SOR cannot be used to realistically characterize the extent of nitrogen
474 and sulfur oxidation during transport-dominated pollution cases, as upstream aging
475 aerosols can significantly increase the above ratios (Ji et al., 2018). In the following
476 discussion, we will focus on the formation mechanism of SNA during different dust
477 stages.

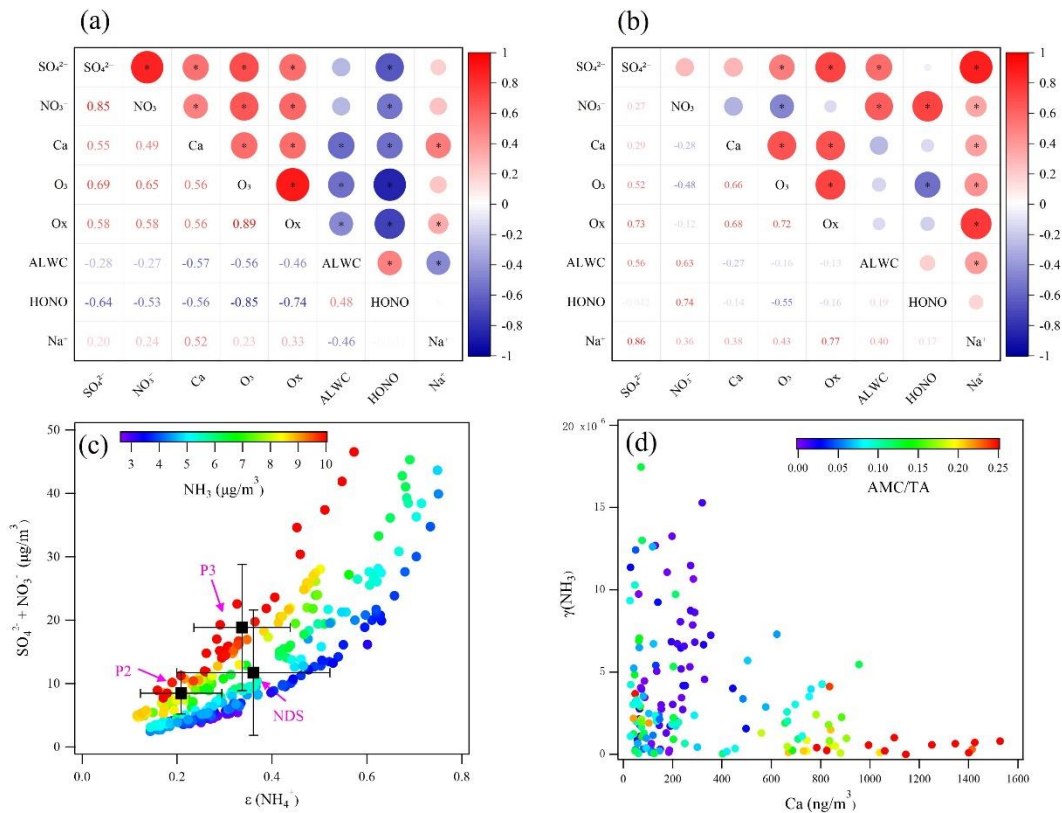
478 The results of SOC/OC ratios differed from the above analysis that SOC/OC was
479 lower during P3 than during P2 and NDS (Figure 6e), suggesting that the formation of
480 secondary organic aerosols was not favored via the dust backflow. This may be due to
481 its maritime transport pathway as the emission intensity of volatile organic compounds
482 from the ocean is much lower than that from land sources. Consequently, the lacking of
483 organic aerosol precursors could be the main cause for the lower SOC/OC ratios during
484 P3. Finally, the $\text{Ca}^{2+}/\text{NH}_4^+$ ratio was employed to assess the relative contributions of
485 alkaline chemical components (Figure 6f). As expected, this ratio during the two dust
486 stages was much higher than that of NDS, indicating the important contribution of dust
487 to alkaline metal ions. The $\text{Ca}^{2+}/\text{NH}_4^+$ ratio was higher during P3 (0.15) than during P2

488 (0.10), which aligned with the findings presented in Section 3.2.

489

490 **3.4.2. Distinct formation processes of secondary aerosols between P2 and P3**

491



492

493 Figure 7. Correlation heatmaps during (a) P2 and (b) P3. The size of dot

494 corresponds to the value of the correlation coefficient. The black star inside the dot

495 means the correlation is significant ($p < 0.05$). (c) The mass concentrations of SO_4^{2-} and

496 NO_3^- as a function of $\epsilon(NH_4^+)$, with dots colored by the concentration of NH_3 . The

497 mean states of P2, P3, and NDS are added. Error bars denote one standard deviations.

498 (d) The uptake coefficient of NH_3 (γ_{NH_3}) on particles as a function of Ca, with dots

499 colored by the AMC/TA molar ratios. AMC and TA denote the total molar

500 concentrations of Na^+ , K^+ , Mg^{2+} , and Ca^{2+} and the total molar concentrations of anions,

501 respectively.

502

503 In this section, we further analyze the formation mechanism and key influencing
504 factors of secondary components during P2 and P3. Figure 7a & 7b compare the
505 correlation heatmaps of SO_4^{2-} and NO_3^- with various parameters. During P2, both SO_4^{2-}
506 and NO_3^- displayed the most significant correlations with O_3 and Ox (O_3+NO_2), while
507 even negatively correlated with ALWC. In regard of the obvious ozone enhancement
508 phenomenon as discussed in Section 3.3.1, the photochemistry pathway for the
509 secondary aerosol formation (e.g., $\text{S(IV)} + \text{O}_3 (\text{aq}) \rightarrow \text{S(VI)}$) should overwhelm over
510 the aqueous phase pathways, e.g., oxidation by H_2O_2 , catalysis by tracer metals, and
511 oxidation by NO_2 . In addition, SO_4^{2-} and NO_3^- also showed moderate correlations with
512 elemental Ca, suggesting that dust acted as a carrier to transport these salts, which can
513 be derived from background minerals in dust (Wu et al., 2022) and dust heterogeneous
514 reactions during the transport (Huang et al., 2010).

515 As for P3, it showed a distinctly different correlation heatmap from P2. While
516 SO_4^{2-} still demonstrates a correlation with O_3 , the relationship between NO_3^- and O_3 (as
517 well as Ox) disappeared. On the contrary, both SO_4^{2-} and NO_3^- show significant
518 correlations with ALWC. During P3, the average RH reached 76%, providing favorable
519 conditions for liquid-phase reactions. Furthermore, by relating NO_3^- and the
520 multiplication of ALWC and NO_2 , the correlation coefficient ($R^2 = 0.41$) was further
521 improved (Figure S4a). Similar results were observed by relating NO_3^- to the
522 multiplication of ALWC and $\text{NO}_2 \cdot \text{O}_3 \cdot \text{NO}_2$ (a proxy of N_2O_5 , (Huang et al., 2021))
523 (Figure S4b), confirming the dominant reaction pathway of nitrogen oxides to nitrate
524 via the aqueous phase reactions. As a result, NO_3^- was also strongly correlated with
525 HONO (Figure S4c), typically deriving from the heterogeneous reactions of NO_2 on

526 the surface of moist particles (Alicke et al. (2002).

527 In addition, unlike P2, both SO_4^{2-} and NO_3^- showed moderate to significant
528 correlations with Na^+ , a tracer of sea salts (Figure 7b). Since neither SO_4^{2-} nor NO_3^-
529 correlated with Ca, it can be inferred that sea salts played a more important role in the
530 transport of air pollutant during the dust backflow over the ocean. To assess whether
531 dust or sea salts participated in the heterogeneous reactions of secondary aerosol during
532 P3, the ISORROPIA II model was run with different scenarios. Figure S5 shows the
533 model performance for SO_4^{2-} , NO_3^- , NH_4^+ , and NH_3 based on the
534 SO_4^{2-} - NO_3^- - NH_4^+ - Cl^- - NH_3 - HCl - HNO_3 system. After adding Ca^{2+} into this
535 thermodynamic equilibrium system, the correlations between the simulations vs
536 observations for all four species were lowered with different extents (Figure S6). If Na^+
537 was added into the thermodynamic equilibrium system, the model performance was
538 slightly improved (Figure S7). This corroborated that the heterogeneous reactions on
539 dust were very limited while sea salts were intensively involved in the formation of
540 secondary inorganic aerosols during the dust backflow.

541 To further explore the influencing factors affecting the formation of secondary
542 inorganic aerosols, we examined the role of NH_3 in different stages, representing by the
543 relationship between the gas-particle partitioning of ammonia ($\varepsilon(\text{NH}_4^+)$), defined as the
544 ratio between particle phase ammonia (NH_4^+) and total ammonia ($\text{NH}_x = \text{NH}_3 + \text{NH}_4^+$)
545 and the total acids ($\text{SO}_4^{2-} + \text{NO}_3^-$). As shown in Figure 7c, it is obvious that the total
546 acids strongly co-varied with $\varepsilon(\text{NH}_4^+)$. Higher $\varepsilon(\text{NH}_4^+)$ resulted in higher
547 concentrations of secondary aerosols. Moreover, under similar $\varepsilon(\text{NH}_4^+)$ conditions,
548 higher NH_3 promoted stronger formation of secondary aerosols. Thus, both NH_3 and
549 $\varepsilon(\text{NH}_4^+)$ collectively determined the aerosol formation potential. The mean states of

550 P2, P3, and NDS are compared in Figure 7c. P2 had the lowest $\epsilon(\text{NH}_4^+)$ with the mean
551 value of 0.21, despite the relatively high concentrations of NH_3 during this period (7.9
552 $\pm 1.0 \mu\text{g}/\text{m}^3$). The relatively low gas-particle partitioning of ammonia limited the
553 neutralization of the acidic components. In contrast, NH_3 during P3 was the highest
554 during the study period ($9.8 \pm 1.8 \mu\text{g}/\text{m}^3$), and $\epsilon(\text{NH}_4^+)$ (0.34) was only slightly lower
555 than that during NDS, thus effectively fostering the formation of secondary inorganic
556 aerosols.

557 To explain this phenomenon, the uptake coefficient of NH_3 (γ_{NH_3}) on particles,
558 which is one of the important parameters affecting the gas-particle partitioning of
559 ammonia, was calculated. Figure 7d shows the decreasing trend of γ_{NH_3} with the
560 increase of dust intensity (using Ca as an indicator). This coincided with a multi-year
561 observational study in Beijing and Shijiazhuang, where γ_{NH_3} obviously increased due
562 to significant decline in alkali earth metal contents from the dust emission sources
563 during 2018 – 2020 (Liu et al., 2022). Thus, this partially explained why $\epsilon(\text{NH}_4^+)$ was
564 relatively low during P2, which was ascribed to the reduced uptake capacity of NH_3 on
565 particles.

566 The ion balance calculation indicated that the total anions and cations are in ideal
567 equilibrium (Figure S8, regression slope = 0.99, $R^2 = 0.99$), indicating that both NH_4^+
568 and alkali metal cations (including Na^+ , K^+ , Mg^{2+} , and Ca^{2+}) contributed to the
569 neutralization of acids to varying degrees. The ratio of alkali metal cations/total anions
570 (AMC/TA) was used to color the data points in Figure 7d, showing an opposite trend
571 between AMC/TA and γ_{NH_3} . During P2, the mean value of AMC/TA reached 21%,
572 implying that the neutralization of acids by NH_3 had been significantly suppressed, thus
573 explaining the decrease in the NH_3 uptake coefficient at high dust intensity. In contrast,

574 the AMC/TA ratio decreased to 11% during P3, indicating a reduced competition
575 between NH₃ and the alkali dust components. Finally, we also compared the aerosol pH
576 at different stages, which was 3.2, 3.0, and 2.8 during P2, P3, and NDS, respectively.
577 The relatively high aerosol acidity at P3 and NDS favored the uptake of alkaline gases
578 (Liu et al., 2022), which also contributed to the higher (γ_{NH_3}) at these two stages.

579

580 **3.5. Estimation of transported and secondarily formed particles during P3**

581 As discussed in previous sections, the aerosols observed during P3 could originate
582 from both aged aerosols transported via the dust backflows and secondary formation.
583 In this section, we aimed to estimate the contribution of transport and secondary
584 formation to the main aerosol species, respectively, based on the simultaneous
585 measurements at the Pudong site and the Lianyungang site. As discussed in Section
586 3.4.1, Lianyungang acted as an upstream region where dust drifted away from the
587 mainland. The duration of dust observed at Lianyungang was approximately from 5:00
588 on October 30 to 16:00 on October 31, about 46 hours ahead of the dust invasion
589 observed at Pudong (Figure S2).

590 To assess the extents of transported air pollutants, black carbon (BC) was used as
591 a reference aerosol component. As shown in Figure S9, one BC pollution episode on
592 October 30 at Lianyungang was observed. Correspondingly, another BC pollution
593 episode emerged at Pudong on November 2 after about 46 hours. Since the air mass
594 trajectory from Lianyungang to Pudong predominantly traversed over the ocean, and
595 considering that BC has no secondary sources, it can be reasonably assumed that the
596 differences of BC concentrations between these two sites were ascribed to the removal
597 processes of particles.

598 To determine the removal fractions of aerosols during dust transport, we first
 599 defined the average concentrations of various aerosol components during the preceding
 600 five hours of the dust at Pudong as their background concentrations. Then, a coefficient
 601 k was derived to calculate the removal fractions of aerosols during the dust transport as
 602 below.

603

$$604 \quad k = \frac{AV_{LYG,BC} - (AV_{PD,BC} - BKG_{PD,BC})}{AV_{LYG,BC}} \quad (3)$$

606 $AV_{LYG,BC}$ and $AV_{PD,BC}$ represent the average concentration of BC at Lianyungang
 607 and Pudong during their respective dust period. $BKG_{PD,BC}$ represents the background
 608 concentration of BC at Pudong. Assuming that other aerosol species were removed with
 609 a similar efficiency as BC, the amounts of transported aerosol species from
 610 Lianyungang to Pudong can be estimated as below.

$$611 \quad TP_{PD,i} = AV_{LYG,i} \times (1 - k) \quad (4)$$

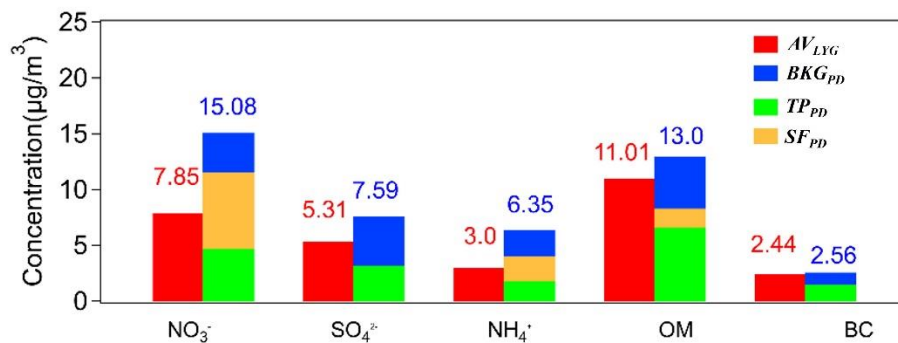
612 $TP_{PD,i}$ represents the transported amounts of aerosol species i . $1 - k$ represents the
 613 transport fraction of aerosols. Then, the secondarily formed aerosol species i at Pudong
 614 can be calculated as below.

$$615 \quad SF_{PD,i} = AV_{PD,i} - BKG_{PD,i} - TP_{PD,i} \quad (5)$$

616 Figure 8 shows the results of the transported and the secondarily formed aerosol
 617 species during P3. It was calculated that the secondarily formed and transported NO_3^-
 618 averaged $6.8 \mu\text{g}/\text{m}^3$ and $4.7 \mu\text{g}/\text{m}^3$, accounting for about 45% and 31% of its total mass
 619 concentration, respectively. This was consistent with the earlier analysis that a
 620 considerable portion of nitrate was formed through the aqueous phase secondary
 621 formation. In contrast, it was calculated that the transported SO_4^{2-} accounted for about

622 42% of its total mass concentration, while the secondarily formed SO_4^{2-} was almost
 623 negligible. This was also consistent with the phenomenon that SO_4^{2-} correlated
 624 significantly with Na^+ (Figure 6b). As for NH_4^+ , it exhibited a similar apportionment as
 625 NO_3^- , with the secondarily formed and transported NH_4^+ accounting for about 35% and
 626 28% of its total mass concentration, respectively. Compared to NO_3^- and NH_4^+ , OM was
 627 more dominated by transport (57%) while its secondary formation only accounted for
 628 about 13%. It should be noted that the simple method devised in this study may have
 629 inherent uncertainties. Considering the prolonged duration of the dust event, it is
 630 possible that certain dust particles lingered over the open ocean. Consequently, the
 631 contributions attributed to aerosol transport should be considered as a conservative
 632 estimate or lower bound, rather than an exhaustive assessment.

633
 634
 635



636

637 Figure 8. The apportioned concentrations of the major aerosol species during P3.

638

639 4. Conclusion

640 During October 29 to November 2, 2019, a long-lasting dust event was observed in
 641 Shanghai based on a synergy measurement of near surface air pollutants, aerosol lidar,

642 wind profiling lidar, and air masses trajectory modeling. Different from most dust
643 events, this dust event was characterized of exceptionally high relative humidity, low
644 wind speed, and relatively high concentrations of gaseous pollutants. The dust event
645 was divided into three stages from P1 – P3. P1 was a short dust episode due to the
646 strong cold front. P2 was a dust episode when RH was moderately high of $70 \pm 26\%$
647 and the southeasterlies prevailed with partial air masses from coastal regions. P3 was a
648 rarely observed dust backflow transport episode. The air masses originated from the
649 Shandong Peninsula and the northern region of Jiangsu province, and then migrated
650 over the Yellow Sea and the East China Sea. RH reached the highest of $76 \pm 24\%$ among
651 the three stages of the dust event.

652 During P2, abnormally high O_3 concentrations were observed, which could be due
653 to the weak synoptic system as well as down drafted high-altitude O_3 along with the
654 subsidence of dust particles Sulfate and nitrate moderately correlated with O_3 while had
655 almost no correlation with ALWC, indicating that the formation of secondary aerosols
656 during P2 should be mainly promoted via the gas-phase oxidations. During P3, a special
657 phenomenon of dust backflow was observed and confirmed by various evidences. The
658 highest Ca^{2+}/Ca ratio was observed due to that the lingerer of dust plumes over the open
659 ocean. Moreover, contributions of V and Ni significantly increased, indicating the
660 mixing between dust and marine vessel emissions. Different from P2, nitrate
661 significantly correlated with ALWC but not with O_3 , indicating its aqueous-phase
662 reaction pathway. Also, sulfate and nitrate exhibited moderate to strong correlations
663 with Na^+ , suggesting sea salts as a medium for the heterogeneous reactions.

664 By analyzing various chemical tracers, the formation extent of SNA was found
665 much stronger during P3 than during P2. Both NH_3 and $\varepsilon(NH_4^+)$

666 $(\text{NH}_4^+ / (\text{NH}_3 + \text{NH}_4^+))$ determined the concentrations of SNA. To explain the relatively
667 high $\varepsilon(\text{NH}_4^+)$ values during P3, the uptake coefficient of NH_3 (γ_{NH_3}) on particles is
668 calculated. γ_{NH_3} negatively varied with the intensity of dust, which were attributed to
669 two factors. Higher contributions of alkali metal components suppressed the
670 neutralization capacity of NH_3 on acids, thereby lowering γ_{NH_3} during P2. Also,
671 relatively high aerosol pH during P2 didn't facilitate the uptake of NH_3 and the
672 subsequent aerosol formation.

673 Based on a simplified method, the amounts of transported and secondarily formed
674 particles during P3 were quantified. It was calculated that about 45% and 31% of NO_3^-
675 was contributed by secondary formation and transport, respectively. In contrast, the
676 transported SO_4^{2-} accounted for about 42% of its total mass concentration while the rest
677 was from its background concentration with negligible secondary formation. OM was
678 dominated by transport (57%) while its secondary formation only accounted for about
679 13%.

680

681 **Data Availability Statement**

682 All data used in this study can be requested upon the corresponding author
683 (huangkan@fudan.edu.cn).

684

685 **Author contributions**

686 KH, QF, and YD designed this study. JH, FY, YL, and JC performed data
687 collection. DL and KH performed data analysis and wrote the paper. All have
688 commented on and reviewed the paper.

689

690 **Competing interests**

691 The authors declare that they have no conflict of interest.

692

693 **Acknowledgments**

694 This work was financially supported by the National Key R&D Plan programs
695 (2023YFE0102500) and National Science Foundation of China (42175119).

696

697

698 **References**

699 Alicke, B., Platt, U., and Stutz, J.: Impact of nitrous acid photolysis on the total hydroxyl
700 radical budget during the Limitation of Oxidant Production/Pianura Padana Produzione di
701 Ozono study in Milan, *J. Geophys. Res.-Atmos.*, 107, 18, 10.1029/2000jd000075, 2002.

702 Ansari, A. S. and Pandis, S. N.: An analysis of four models predicting the partitioning of
703 semivolatile inorganic aerosol components, *Aerosol Science And Technology*, 31, 129-153,
704 10.1080/027868299304200, 1999.

705 Arimoto, R., Ray, B. J., Lewis, N. F., Tomza, U., and Duce, R. A.: Mass-particle size
706 distributions of atmospheric dust and the dry deposition of dust to the remote ocean, *J. Geophys.*
707 *Res.-Atmos.*, 102, 15867-15874, 10.1029/97jd00796, 1997.

708 Barkley, A., Olson, N., Prospero, J., Gatineau, A., Panechou, K., Maynard, N.,
709 Blackwelder, P., China, S., Ault, A., and Gaston, C.: Atmospheric Transport of North African
710 Dust - Bearing Supermicron Freshwater Diatoms to South America: Implications for Iron
711 Transport to the Equatorial North Atlantic Ocean, *Geophysical Research Letters*, 48,
712 10.1029/2020GL090476, 2021.

713 Becagli, S., Sferlazzo, D. M., Pace, G., di Sarra, A., Bommarito, C., Calzolari, G., Ghedini,
714 C., Lucarelli, F., Meloni, D., Monteleone, F., Severi, M., Traversi, R., and Udisti, R.: Evidence
715 for heavy fuel oil combustion aerosols from chemical analyses at the island of Lampedusa: a
716 possible large role of ships emissions in the Mediterranean, *Atmos. Chem. Phys.*, 12, 3479-
717 3492, 10.5194/acp-12-3479-2012, 2012.

718 Benas, N., Mourtzanou, E., Kouvarakis, G., Bais, A., Mihalopoulos, N., and Vardavas, I.:
719 Surface ozone photolysis rate trends in the Eastern Mediterranean: Modeling the effects of
720 aerosols and total column ozone based on Terra MODIS data, *Atmospheric Environment*, 74,
721 1-9, 10.1016/j.atmosenv.2013.03.019, 2013.

722 Bernard, F., Cazaunau, M., Gosselin, B., Zhou, B., Zheng, J., Liang, P., Zhang, Y., Ye, X.,

723 Daële, V., Mu, Y., Zhang, R., Chen, J., and Mellouki, A.: Measurements of nitrous acid (HONO)
724 in urban area of Shanghai, China, *Environmental Science and Pollution Research*, 23, 5818-
725 5829, 10.1007/s11356-015-5797-4, 2016.

726 Bozlaker, A., Prospero, J. M., Price, J., and Chellam, S.: Identifying and Quantifying the
727 Impacts of Advected North African Dust on the Concentration and Composition of Airborne
728 Fine Particulate Matter in Houston and Galveston, Texas, *J Geophys Res-Atmos*, 124, 12282-
729 12300, 10.1029/2019jd030792, 2019.

730 Cwiertny, D. M., Baltrusaitis, J., Hunter, G. J., Laskin, A., Scherer, M. M., and Grassian,
731 V. H.: Characterization and acid-mobilization study of iron-containing mineral dust source
732 materials, *J Geophys Res-Atmos*, 113, Artn D05202
733 10.1029/2007jd009332, 2008.

734 Dall'Osto, M., Harrison, R. M., Coe, H., and Williams, P.: Real-time secondary aerosol
735 formation during a fog event in London, *Atmospheric Chemistry And Physics*, 9, 2459-2469,
736 10.5194/acp-9-2459-2009, 2009.

737 Draxler, R. R., and G. D. Hess, 1998: An overview of the HYSPLIT_4 modeling
738 system for trajectories, dispersion, and deposition. *Aust. Meteor. Mag.*, 47, 295–308.

739 Fan, H., Zhao, C., Yang, Y., and Yang, X.: Spatio-Temporal Variations of the
740 PM_{2.5}/PM₁₀ Ratios and Its Application to Air Pollution Type Classification in China, *Frontiers*
741 *in Environmental Science*, 2021, <https://doi.org/10.3389/fenvs.2021.692440>.

742

743 Fan, Q. Z., Zhang, Y., Ma, W. C., Ma, H. X., Feng, J. L., Yu, Q., Yang, X., Ng, S. K. W.,
744 Fu, Q. Y., and Chen, L. M.: Spatial and Seasonal Dynamics of Ship Emissions over the Yangtze
745 River Delta and East China Sea and Their Potential Environmental Influence, *Environmental*
746 *Science & Technology*, 50, 1322-1329, 10.1021/acs.est.5b03965, 2016.

747 Feng, X., Mao, R., Gong, D.-Y., Zhao, C., Wu, C., Zhao, C., Wu, G., Lin, Z., Liu, X., Wang,
748 K., and Sun, Y.: Increased Dust Aerosols in the High Troposphere Over the Tibetan Plateau
749 From 1990s to 2000s, *Journal of Geophysical Research: Atmospheres*, 125, e2020JD032807,
750 <https://doi.org/10.1029/2020JD032807>, 2020.

751 Ge, X. L., He, Y. A., Sun, Y. L., Xu, J. Z., Wang, J. F., Shen, Y. F., and Chen, M. D.:
752 Characteristics and Formation Mechanisms of Fine Particulate Nitrate in Typical Urban Areas
753 in China, *Atmosphere*, 8, 12, 10.3390/atmos8030062, 2017.

754 Ginoux, P., Prospero, J. M., Torres, O., and Chin, M.: Long-term simulation of global dust
755 distribution with the GOCART model: correlation with North Atlantic Oscillation,
756 *Environmental Modelling & Software*, 19, 113-128, [https://doi.org/10.1016/S1364-](https://doi.org/10.1016/S1364-8152(03)00114-2)
757 [8152\(03\)00114-2](https://doi.org/10.1016/S1364-8152(03)00114-2), 2004.

758 Goodman, M. M., Carling, G. T., Fernandez, D. P., Rey, K. A., Hale, C. A., Bickmore, B.

759 R., Nelson, S. T., and Munroe, J. S.: Trace element chemistry of atmospheric deposition along
760 the Wasatch Front (Utah, USA) reflects regional playa dust and local urban aerosols, *Chemical*
761 *Geology*, 530, 10.1016/j.chemgeo.2019.119317, 2019.

762 Hammond, D. M., Dvonch, J. T., Keeler, G. J., Parker, E. A., Kamal, A. S., Barres, J. A.,
763 Yip, F. Y., and Brakefield-Caldwell, W.: Sources of ambient fine particulate matter at two
764 community sites in Detroit, Michigan, *Atmos. Environ.*, 42, 720-732,
765 10.1016/j.atmosenv.2007.09.065, 2008.

766 Hertel, O., Skjoth, C. A., Reis, S., Bleeker, A., Harrison, R. M., Cape, J. N., Fowler, D.,
767 Skiba, U., Simpson, D., Jickells, T., Kulmala, M., Gyldenkaerne, S., Sorensen, L. L., Erisman,
768 J. W., and Sutton, M. A.: Governing processes for reactive nitrogen compounds in the European
769 atmosphere, *Biogeosciences*, 9, 4921-4954, 10.5194/bg-9-4921-2012, 2012.

770 Hilario, M. R. A., Cruz, M. T., Cambaliza, M. O. L., Reid, J. S., Xian, P., Simpas, J. B.,
771 Lagrosas, N. D., Uy, S. N. Y., Cliff, S., and Zhao, Y. J.: Investigating size-segregated sources
772 of elemental composition of particulate matter in the South China Sea during the 2011 Vasco
773 cruise, *Atmospheric Chemistry And Physics*, 20, 1255-1276, 10.5194/acp-20-1255-2020, 2020.

774 Hsu, S.-C., Lee, C. S. L., Huh, C.-A., Shaheen, R., Lin, F.-J., Liu, S. C., Liang, M.-C., and
775 Tao, J.: Ammonium deficiency caused by heterogeneous reactions during a super Asian dust
776 episode, *Journal of Geophysical Research: Atmospheres*, 119, 6803-6817,
777 10.1002/2013jd021096, 2014.

778 Huang, K., Fu, J. S., Lin, N.-H., Wang, S.-H., Dong, X., and Wang, G.: Superposition of
779 Gobi Dust and Southeast Asian Biomass Burning: The Effect of Multisource Long-Range
780 Transport on Aerosol Optical Properties and Regional Meteorology Modification, *Journal of*
781 *Geophysical Research: Atmospheres*, 124, 9464-9483, <https://doi.org/10.1029/2018JD030241>,
782 2019.

783 Huang, K., Zhuang, G., Li, J., Wang, Q., Sun, Y., Lin, Y., and Fu, J. S.: Mixing of Asian
784 dust with pollution aerosol and the transformation of aerosol components during the dust storm
785 over China in spring 2007, *Journal of Geophysical Research*, 115, 10.1029/2009jd013145, 2010.

786 Huang, X., Ding, A. J., Gao, J., Zheng, B., Zhou, D. R., Qi, X. M., Tang, R., Wang, J. P.,
787 Ren, C. H., Nie, W., Chi, X. G., Xu, Z., Chen, L. D., Li, Y. Y., Che, F., Pang, N. N., Wang, H.
788 K., Tong, D., Qin, W., Cheng, W., Liu, W. J., Fu, Q. Y., Liu, B. X., Chai, F. H., Davis, S. J.,
789 Zhang, Q., and He, K. B.: Enhanced secondary pollution offset reduction of primary emissions
790 during COVID-19 lockdown in China, *Natl Sci Rev*, 8, ARTN nwaal37
791 10.1093/nsr/nwaa137, 2021.

792 Jeong, G. Y.: Bulk and single-particle mineralogy of Asian dust and a comparison with its
793 source soils, *J Geophys Res-Atmos*, 113, Artn D02208
794 10.1029/2007jd008606, 2008.

795 Ji, Y., Qin, X. F., Wang, B., Xu, J., Shen, J. D., Chen, J. M., Huang, K., Deng, C. R., Yan,
796 R. C., Xu, K. E., and Zhang, T.: Counteractive effects of regional transport and emission control
797 on the formation of fine particles: a case study during the Hangzhou G20 summit, *Atmos Chem*
798 *Phys*, 18, 13581-13600, 10.5194/acp-18-13581-2018, 2018.

799 Jiang, Y., Zhuang, G., Wang, Q., Huang, K., Deng, C., Yu, G., Xu, C., Fu, Q., Lin, Y., Fu,
800 J. S., Li, M., and Zhou, Z.: Impact of mixed anthropogenic and natural emissions on air quality
801 and eco-environment—the major water-soluble components in aerosols from northwest to
802 offshore isle, *Air Quality, Atmosphere & Health*, 11, 521-534, 10.1007/s11869-018-0557-5,
803 2018.

804 Laskin, A., Wietsma, T. W., Krueger, B. J., and Grassian, V. H.: Heterogeneous chemistry
805 of individual mineral dust particles with nitric acid: A combined CCSEM/EDX, ESEM, and
806 ICP-MS study, *J Geophys Res-Atmos*, 110, ArtD10208
807 10.1029/2004jd005206, 2005.

808 Li, T., Wang, Y., Zhou, J., Wang, T., Ding, A. J., Nie, W., Xue, L. K., Wang, X. F., and
809 Wang, W. X.: Evolution of trace elements in the planetary boundary layer in southern China:
810 Effects of dust storms and aerosol-cloud interactions, *J Geophys Res-Atmos*, 122, 3492-3506,
811 10.1002/2016jd025541, 2017.

812 Liang, Y., Liu, Y., Wang, H., Li, L., Duan, Y., and Lu, K.: Regional characteristics of
813 ground-level ozone in Shanghai based on PCA analysis, *Acta Scientiae Circumstantiae*, 38,
814 3807-3815, 2018.

815 Liu, H., Liu, S., Xue, B., Lv, Z., Meng, Z., Yang, X., Xue, T., Yu, Q., and He, K.: Ground-
816 level ozone pollution and its health impacts in China, *Atmospheric Environment*, 173, 223-230,
817 <https://doi.org/10.1016/j.atmosenv.2017.11.014>, 2018.

818 Liu, J., Ding, J., Rexiding, M., Li, X., Zhang, J., Ran, S., Bao, Q., and Ge, X.:
819 Characteristics of dust aerosols and identification of dust sources in Xinjiang, China,
820 *Atmospheric Environment*, 262, 118651, <https://doi.org/10.1016/j.atmosenv.2021.118651>,
821 2021.

822 Liu, Y. C., Zhan, J. L., Zheng, F. X., Song, B. Y., Zhang, Y. S., Ma, W., Hua, C. J., Xie, J.
823 L., Bao, X. L., Yan, C., Bianchi, F., Petaja, T., Ding, A. J., Song, Y., He, H., and Kulmala, M.:
824 Dust emission reduction enhanced gas-to-particle conversion of ammonia in the North China
825 Plain, *Nat Commun*, 13, ARTN 6887
826 10.1038/s41467-022-34733-4, 2022.

827 Ma, S. Q., Zhang, X. L., Gao, C., Tong, Q. S., Xiu, A. J., Zhao, H. M., and Zhang, S. C.:
828 Simulating Performance of CHIMERE on a Late Autumnal Dust Storm over Northern China,
829 *Sustainability-Basel*, 11, ARTN 1074
830 10.3390/su11041074, 2019.

831 Malm, W. C., Sisler, J. F., Huffman, D., Eldred, R. A., and Cahill, T. A.: Spatial and
832 seasonal trends in particle concentration and optical extinction in the United States, *Journal of*
833 *Geophysical Research: Atmospheres*, 99, 1347-1370, <https://doi.org/10.1029/93JD02916>, 1994.

834 Mcneil, W. R. and Carswell, A. I.: Lidar Polarization Studies of Troposphere, *Appl.*
835 *Opt.*, 14, 2158–2168, 1975.

836 Mentel, T. F., Bleilebens, D., and Wahner, A.: A study of nighttime nitrogen oxide
837 oxidation in a large reaction chamber—the fate of NO₂, N₂O₅, HNO₃, and O₃ at different
838 humidities, *Atmospheric Environment*, 30, 4007-4020, [https://doi.org/10.1016/1352-](https://doi.org/10.1016/1352-2310(96)00117-3)
839 [2310\(96\)00117-3](https://doi.org/10.1016/1352-2310(96)00117-3), 1996.

840 Nagashima, K., Suzuki, Y., Irino, T., Nakagawa, T., Tada, R., Hara, Y., Yamada, K., and
841 Kurosaki, Y.: Asian dust transport during the last century recorded in Lake Suigetsu sediments,
842 *Geophysical Research Letters*, 43, 2835-2842, <https://doi.org/10.1002/2015GL067589>, 2016.

843 Nenes, A., Pandis, S. N., and Pilinis, C.: ISORROPIA: A new thermodynamic equilibrium
844 model for multiphase multicomponent inorganic aerosols, *Aquat. Geochem.*, 4, 123-152,
845 10.1023/a:1009604003981, 1998.

846 Patel, A. and Rastogi, N.: Chemical Composition and Oxidative Potential of Atmospheric
847 PM₁₀ over the Arabian Sea, *ACS Earth Space Chem.*, 4, 112-121,
848 10.1021/acsearthspacechem.9b00285, 2020.

849 Perez, N., Pey, J., Reche, C., Cortes, J., Alastuey, A., and Querol, X.: Impact of harbour
850 emissions on ambient PM₁₀ and PM_{2.5} in Barcelona (Spain): Evidences of secondary aerosol
851 formation within the urban area, *Science Of the Total Environment*, 571, 237-250,
852 10.1016/j.scitotenv.2016.07.025, 2016.

853 Petetin, H., Sciare, J., Bressi, M., Gros, V., Rosso, A., Sanchez, O., Sarda-Estève, R., Petit,
854 J. E., and Beekmann, M.: Assessing the ammonium nitrate formation regime in the Paris
855 megacity and its representation in the CHIMERE model, *Atmos. Chem. Phys.*, 16, 10419-
856 10440, 10.5194/acp-16-10419-2016, 2016.

857 Shen, L., Zhao, C., Ma, Z., Li, Z., Li, J., and Wang, K.: Observed decrease of summer sea-
858 land breeze in Shanghai from 1994 to 2014 and its association with urbanization, *Atmospheric*
859 *Research*, 227, 198-209, <https://doi.org/10.1016/j.atmosres.2019.05.007>, 2019.

860 Shimizu, A., N. Sugimoto, I. Matsui, K. Arao, I. Uno, T. Murayama, N. Kagawa,
861 K. Aoki, A. Uchiyama, and A. Yamazaki (2004), Continuous observations of Asian dust
862 and other aerosols by polarization lidars in China and Japan during ACE-Asia, *J.*
863 *Geophys. Res.*, 109, D19S17, doi:10.1029/ 2002JD003253.

864 Song, S., Gao, M., Xu, W., Shao, J., Shi, G., Wang, S., Wang, Y., Sun, Y., and McElroy, M.
865 B.: Fine-particle pH for Beijing winter haze as inferred from different thermodynamic
866 equilibrium models, *Atmos. Chem. Phys.*, 18, 7423-7438, 10.5194/acp-18-7423-2018, 2018.

867 Stein, A. F., Draxler, R. R., Rolph, G. D., Stunder, B. J. B., Cohen, M. D., Ngan,
868 F., NOAA's HYSPLIT Atmospheric Transport and Dispersion Modeling System,
869 Bulletin of the American Meteorological Society, 2015, 2059–2077.

870 Su, L., Yuan, Z., Fung, J. C. H., and Lau, A. K. H.: A comparison of HYSPLIT backward
871 trajectories generated from two GDAS datasets, Science of The Total Environment, 506-507,
872 527-537, <https://doi.org/10.1016/j.scitotenv.2014.11.072>, 2015.

873 Sun, P., Nie, W., Wang, T., Chi, X., Huang, X., Xu, Z., Zhu, C., Wang, L., Qi, X., Zhang,
874 Q., and Ding, A.: Impact of air transport and secondary formation on haze pollution in the
875 Yangtze River Delta: In situ online observations in Shanghai and Nanjing, Atmospheric
876 Environment, 225, 117350, <https://doi.org/10.1016/j.atmosenv.2020.117350>, 2020.

877 Tang, M., Cziczo, D. J., and Grassian, V. H.: Interactions of Water with Mineral Dust
878 Aerosol: Water Adsorption, Hygroscopicity, Cloud Condensation, and Ice Nucleation,
879 Chemical Reviews, 116, 4205-4259, 10.1021/acs.chemrev.5b00529, 2016.

880 Tang, M. J., Huang, X., Lu, K. D., Ge, M. F., Li, Y. J., Cheng, P., Zhu, T., Ding, A. J.,
881 Zhang, Y. H., Gligorovski, S., Song, W., Ding, X., Bi, X. H., and Wang, X. M.: Heterogeneous
882 reactions of mineral dust aerosol: implications for tropospheric oxidation capacity, Atmos
883 Chem Phys, 17, 11727-11777, 10.5194/acp-17-11727-2017, 2017.

884 Tian, R., Ma, X., Sha, T., Pan, X., and Wang, Z.: Exploring dust heterogeneous chemistry
885 over China: Insights from field observation and GEOS-Chem simulation, Science of The Total
886 Environment, 798, 149307, <https://doi.org/10.1016/j.scitotenv.2021.149307>, 2021.

887 Vicars, W. C. and Sickman, J. O.: Mineral dust transport to the Sierra Nevada, California:
888 Loading rates and potential source areas, Journal of Geophysical Research, 116,
889 10.1029/2010jg001394, 2011.

890 Wang, G., Chen, J., Xu, J., Yun, L., Zhang, M., Li, H., Qin, X., Deng, C., Zheng, H., Gui,
891 H., Liu, J., and Huang, K.: Atmospheric processing at the sea-land interface over the South
892 China Sea: secondary aerosol formation, aerosol acidity, and role of sea salts, Journal of
893 Geophysical Research: Atmospheres, n/a, e2021JD036255,
894 <https://doi.org/10.1029/2021JD036255>,

895 Wang, G. C., Chen, J., Xu, J., Yun, L., Zhang, M. D., Li, H., Qin, X. F., Deng, C. R., Zheng,
896 H. T., Gui, H. Q., Liu, J. G., and Huang, K.: Atmospheric Processing at the Sea-Land Interface
897 Over the South China Sea: Secondary Aerosol Formation, Aerosol Acidity, and Role of Sea
898 Salts, J. Geophys. Res.-Atmos., 127, 10.1029/2021jd036255, 2022a.

899 Wang, G. H., Cheng, C. L., Huang, Y., Tao, J., Ren, Y. Q., Wu, F., Meng, J. J., Li, J. J.,
900 Cheng, Y. T., Cao, J. J., Liu, S. X., Zhang, T., Zhang, R., and Chen, Y. B.: Evolution of aerosol
901 chemistry in Xi'an, inland China, during the dust storm period of 2013-Part 1: Sources,
902 chemical forms and formation mechanisms of nitrate and sulfate, Atmospheric Chemistry And

903 Physics, 14, 11571-11585, 10.5194/acp-14-11571-2014, 2014.

904 Wang, H. C. and Lu, K. D.: Determination and Parameterization of the Heterogeneous
905 Uptake Coefficient of Dinitrogen Pentoxide (N₂O₅), Prog Chem, 28, 917-933,
906 10.7536/Pc151225, 2016.

907 Wang, J. J., Zhang, M. G., Bai, X. L., Tan, H. J., Li, S., Liu, J. P., Zhang, R., Wolters, M.
908 A., Qin, X. Y., Zhang, M. M., Lin, H. M., Li, Y. N., Li, J., and Chen, L. Q.: Large-scale transport
909 of PM_{2.5} in the lower troposphere during winter cold surges in China, Sci Rep, 7, 10,
910 10.1038/s41598-017-13217-2, 2017.

911 Wang, L., Du, H., Chen, J., Zhang, M., Huang, X., Tan, H., Kong, L., and Geng, F.:
912 Consecutive transport of anthropogenic air masses and dust storm plume: Two case events at
913 Shanghai, China, Atmospheric Research, 127, 22-33,
914 <https://doi.org/10.1016/j.atmosres.2013.02.011>, 2013.

915 Wang, N., Zheng, P., Wang, R., Wei, B., An, Z., Li, M., Xie, J., Wang, Z., Wang, H., and
916 He, M.: Homogeneous and heterogeneous atmospheric ozonolysis of acrylonitrile on the
917 mineral dust aerosols surface, Journal of Environmental Chemical Engineering, 9, 106654,
918 <https://doi.org/10.1016/j.jece.2021.106654>, 2021.

919 Wang, Q., Wang, X., Huang, R., Wu, J., Xiao, Y., Hu, M., Fu, Q., Duan, Y., and Chen, J.-
920 M.: Regional Transport of PM_{2.5} and O₃ Based on Complex Network Method and Chemical
921 Transport Model in the Yangtze River Delta, China, Journal of Geophysical Research:
922 Atmospheres, 127, 10.1029/2021JD034807, 2022b.

923 Wang, Z., Pan, X. L., Uno, I., Chen, X. S., Yamamoto, S., Zheng, H. T., Li, J., and Wang,
924 Z. F.: Importance of mineral dust and anthropogenic pollutants mixing during a long-lasting
925 high PM event over East Asia, Environ. Pollut., 234, 368-378, 10.1016/j.envpol.2017.11.068,
926 2018.

927 Wang, Z. L., Huang, X., Wang, N., Xu, J. W., and Ding, A. J.: Aerosol-Radiation
928 Interactions of Dust Storm Deteriorate Particle and Ozone Pollution in East China, J Geophys
929 Res-Atmos, 125, ARTN e2020JD033601
930 10.1029/2020JD033601, 2020.

931 West, J. J., Ansari, A. S., and Pandis, S. N.: Marginal PM_{2.5}: Nonlinear Aerosol Mass
932 Response to Sulfate Reductions in the Eastern United States, Journal of the Air & Waste
933 Management Association, 49, 1415-1424, 10.1080/10473289.1999.10463973, 1999.

934 Wu, C., Zhang, S., Wang, G., Lv, S., Li, D., Liu, L., Li, J., Liu, S., Du, W., Meng, J., Qiao,
935 L., Zhou, M., Huang, C., and Wang, H.: Efficient Heterogeneous Formation of Ammonium
936 Nitrate on the Saline Mineral Particle Surface in the Atmosphere of East Asia during Dust Storm
937 Periods, Environmental Science & Technology, 54, 15622-15630, 10.1021/acs.est.0c04544,
938 2020.

939 Wu, F., Cheng, Y., Hu, T. F., Song, N., Zhang, F., Shi, Z. B., Ho, S. S. H., Cao, J. J., and
940 Zhang, D. Z.: Saltation-Sandblasting Processes Driving Enrichment of Water- Soluble Salts in
941 Mineral Dust, *Environ Sci Tech Let*, 9, 921-928, 10.1021/acs.estlett.2c00652, 2022.

942 Xie, S. D., Yu, T., Zhang, Y. H., Zeng, L. M., Qi, L., and Tang, X. Y.: Characteristics of
943 PM10, SO2, NO, and O-3 in ambient air during the dust storm period in Beijing, *Sci Total*
944 *Environ*, 345, 153-164, 10.1016/j.scitotenv.2004.10.013, 2005.

945 Xu, J., Chen, J., Zhao, N., Wang, G. C., Yu, G. Y., Li, H., Huo, J. T., Lin, Y. F., Fu, Q. Y.,
946 Guo, H. Y., Deng, C. R., Lee, S. H., Chen, J. M., and Huang, K.: Importance of gas-particle
947 partitioning of ammonia in haze formation in the rural agricultural environment, *Atmospheric*
948 *Chemistry and Physics*, 20, 7259-7269, 10.5194/acp-20-7259-2020, 2020.

949 Xu, P., Zhang, J. K., Ji, D. S., Liu, Z. R., Tang, G. Q., Hu, B., Jiang, C. S., and Wang, Y.
950 S.: Evaluating the Effects of Springtime Dust Storms over Beijing and the Associated
951 Characteristics of Sub-Micron Aerosol, *Aerosol Air Qual Res*, 17, 680-692,
952 10.4209/aaqr.2016.05.0195, 2017.

953 Yang, Y., Wang, Z. L., Lou, S. J., Xue, L., Lu, J. P., Wang, H. Y., Wang, J. D., Ding, A. J.,
954 and Huang, X.: Strong ozone intrusions associated with super dust storms in East Asia, *Atmos*
955 *Environ*, 290, ARTN 119355
956 10.1016/j.atmosenv.2022.119355, 2022.

957 Yu, S. C., Dennis, R., Roselle, S., Nenes, A., Walker, J., Eder, B., Schere, K., Swall, J., and
958 Robarge, W.: An assessment of the ability of three-dimensional air quality models with current
959 thermodynamic equilibrium models to predict aerosol NO3, *J. Geophys. Res.-Atmos.*, 110,
960 10.1029/2004jd004718, 2005.

961 Zhang, D., Iwasaka, Y., Shi, G., Zang, J., Hu, M., and Li, C.: Separated status of the natural
962 dust plume and polluted air masses in an Asian dust storm event at coastal areas of China,
963 *Journal of Geophysical Research (Atmospheres)*, 110, D06302, 10.1029/2004jd005305, 2005.

964 Zhang, S. P., Xing, J., Sarwar, G., Ge, Y. L., He, H., Duan, F. K., Zhao, Y., He, K. B., Zhu,
965 L. D., and Chu, B. W.: Parameterization of heterogeneous reaction of SO2 to sulfate on dust
966 with coexistence of NH3 and NO2 under different humidity conditions, *Atmos Environ*, 208,
967 133-140, 10.1016/j.atmosenv.2019.04.004, 2019.

968 Zhang, X. L., Wu, G. J., Zhang, C. L., Xu, T. L., and Zhou, Q. Q.: What is the real role of
969 iron oxides in the optical properties of dust aerosols?, *Atmos Chem Phys*, 15, 12159-12177,
970 10.5194/acp-15-12159-2015, 2015.

971 Zhao, D., Xin, J., Wang, W., Jia, D., Wang, Z., Xiao, H., Liu, C., Zhou, J., Tong, L., Ma,
972 Y., Wen, T.-X., Wu, F.-K., and Wang, L.: Effects of the sea-land breeze on coastal ozone
973 pollution in the Yangtze River Delta, *Science of The Total Environment*, 807,
974 10.1016/j.scitotenv.2021.150306, 2021.

975 Zheng, G. J., Duan, F. K., Su, H., Ma, Y. L., Cheng, Y., Zheng, B., Zhang, Q., Huang, T.,
976 Kimoto, T., Chang, D., Poschl, U., Cheng, Y. F., and He, K. B.: Exploring the severe winter
977 haze in Beijing: the impact of synoptic weather, regional transport and heterogeneous reactions,
978 Atmos Chem Phys, 15, 2969-2983, 10.5194/acp-15-2969-2015, 2015.

979 Zheng, Y., Zhao, T., Che, H., Liu, Y., Han, Y., Liu, C., Xiong, J., Liu, J., and Zhou, Y.: A
980 20-year simulated climatology of global dust aerosol deposition, Science of The Total
981 Environment, 557-558, 861-868, <https://doi.org/10.1016/j.scitotenv.2016.03.086>, 2016.

982